Finite-size effects in photonic-crystal surface-emitting lasers: critical discussion of different approximations

Research Article Vol. 33, No. 25 / 15 Dec 2025 / Optics Express 53098
Optics EXPRESS

Finite-size effects in photonic-crystal surface-emitting lasers: critical discussion of different approximations

LARS PERSSON,[1,*] MORITZ RIEDEL,[2] ÅSA HAGLUND,[1] AND ULRICH THEODOR SCHWARZ[2]

[1]Department of Microtechnology and Nanoscience, Chalmers University of Technology, Gothenburg 41296, Sweden
[2]Institute of Physics, Chemnitz University of Technology, Chemnitz 09126, Germany
[*]lars.persson@chalmers.se

Abstract: We present a comparative study of vertical and lateral loss estimation in photonic-crystal surface-emitting lasers (PCSELs), focusing on how finite-size effects depend on the choice of infinite-structure band model. To analyze these effects, we introduce a k-space weighted loss estimation (kSWLE) framework that can be applied to any infinite-structure band model, and we contrast its predictions with those of finite coupled-wave theory (finite-CWT), which inherently relies on the infinite-CWT bandstructure. The kSWLE approach provides a semi-analytical means of estimating radiative and lateral losses by integrating band-dependent quantities over a Gaussian k-space envelope determined by the device size. We apply kSWLE using both CWT and guided-mode expansion (GME) bandstructure models, enabling a direct comparison of how different infinite-structure descriptions influence the predicted losses and spectral properties. In regimes where the lasing mode is dominated by a single band and has a spectrally compact k-space distribution, kSWLE reproduces similar scaling trends as finite-CWT. However, for small devices or at specific fill factors, the mode has a broader k-space distribution with contributions from multiple bands, leading to ambiguous mode classification and increased deviation between models. These results highlight the strengths and limitations of each modelling strategy and establish kSWLE as a practical tool for evaluating finite-size effects in PCSELs.

1. Introduction

Photonic-crystal surface-emitting lasers (PCSELs) are an emerging class of lasers capable of delivering high output power with high beam quality from a compact, monolithic chip [1]. Their distinguishing feature is the use of a two-dimensional photonic crystal to provide distributed in-plane optical feedback as well as out-of-plane (vertical) coupling to radiative modes, enabling large-area single-mode operation and narrow beam divergence: features typically associated with bulkier laser systems such as gas or solid-state lasers [2]. These attributes make PCSELs highly attractive for a wide range of applications across different wavelength regimes, including laser-based displays, automotive headlights and machining of difficult-to-process materials in the visible range [3], remote sensing and free-space communication in the near-infrared [4], and for disinfection of water, air, and surfaces [5].

The fundamental operating principle of PCSELs relies on coherent coupling of multiple in-plane Bloch waves near the photonic band edge, typically at the Γ-point [6], where the group velocity vanishes. The band-edge effect enables strong in-plane feedback, while the photonic crystal also allows for vertical outcoupling [2]. The resulting modal field forms a standing wave distributed across the photonic-crystal region, enabling high-brightness operation over a large lateral area. While the modal properties of infinite periodic structures can be calculated using coupled-wave theory (CWT) [7,8], guided-mode expansion (GME) [9], rigorous coupled-wave

#580979 https://doi.org/10.1364/OE.580979
Journal © 2025 Received 6 Oct 2025; revised 25 Nov 2025; accepted 25 Nov 2025; published 9 Dec 2025

Optics EXPRESS

analysis (RCWA) [10], effective-index methods [11], or finite-difference time-domain (FDTD) method [12], it is important to note that in infinitely large PCSELs vertical outcoupling is mainly determined by the symmetry of the unit cell. For highly symmetric unit cells (e.g., circular holes), vertical outcoupling at the Γ-point mode is symmetry-forbidden for the low-loss modes, so vertical losses vanish to first order. However, real devices are finite in extent, and the resulting truncation perturbs the field and breaks this symmetry, leading to vertical outcoupling even for symmetry-protected structures [7,8], while at the same time giving rise to additional losses through energy leakage at the lateral device boundaries.

Capturing these finite-size effects is essential to accurately predict the lasing mode and modal discrimination [7,8]. While FDTD can capture these effects, the computational cost increases steeply with device size, making them impractical for realistic PCSEL apertures with diameters of typically several hundred lattice periods [13,14]. An alternative is three-dimensional finite coupled-wave theory (finite-CWT), which accounts for both surface radiation and in-plane losses [7,8]. The method separates the problem into two domains: a reciprocal-space (k-space) unit cell analysis for calculating mode properties near the Γ point, and a real-space finite-difference scheme on a hexagonal grid to capture finite-size effects such as threshold gain, field intensity distributions, and far-field patterns. Being semi-analytical, finite-CWT is highly efficient, with simulations typically completing in a few seconds. This method has been successfully applied to both square- and triangular-lattice PCSELs [7,8,15]. More recently, probabilistic Markov chain (PMC) modeling has also been introduced, where the photonic crystal is represented as a network of scattering sites that redistribute light according to coupling probabilities [16–19]. While this approach can capture redistribution effects, it does not directly track the phase of propagating waves and therefore cannot model interference effects.

In this work, we introduce a semi-analytical framework, k-space weighted loss estimation (kSWLE), as an alternative to finite-CWT for estimating modal losses in finite-size PCSELs. The kSWLE method leverages the observation that for moderately large PCSELs, the k-space distribution of the lasing mode is approximately Gaussian, centered at the Γ-point, with a width determined by the device diameter. This enables vertical and lateral losses to be estimated by integrating the infinite-structure loss and group velocity (band curvature) over the relevant k-space area. kSWLE enables the use of arbitrary infinite-structure models to evaluate finite-size effects. In this work, we apply kSWLE using both CWT- and GME-derived bandstructures, allowing us to examine how the choice of infinite model influences loss predictions. We benchmark kSWLE against finite-CWT simulations and compare both approaches in terms of their ability to predict vertical and lateral losses, as well as the dominant lasing mode. Our goal is to clarify the strengths, limitations, and practical implications of both methods for PCSEL design and optimization. Although we study a UV-C PCSEL operating near 275 nm, with a structure similar to devices recently demonstrated by our groups [20–22], the modeling frameworks used here, finite-CWT and kSWLE, are general and applicable to other lattice geometries and emission wavelengths.

2. PCSEL structure and lattice geometry

This section describes the PCSEL structure used in our simulations. We define the real and reciprocal lattice vectors of the hexagonal photonic crystal and specify relevant material parameters. These definitions establish the foundation for the coupled-wave and guided-mode simulations presented in subsequent sections.

2.1. Photonic crystal lattice and reciprocal vectors

The device structure used in this work is based on the optically pumped UV-C PCSELs recently demonstrated by our groups [20]. A schematic of the PCSEL structure and hexagonal lattice is

Optics EXPRESS

shown in Fig. 1(a). The hexagonal lattice is defined by the real-space primitive lattice vectors

$$\mathbf{a}_1 = \left(\frac{\sqrt{3}a}{2}, -\frac{a}{2}\right), \quad \mathbf{a}_2 = \left(\frac{\sqrt{3}a}{2}, \frac{a}{2}\right), \tag{1}$$

where a is the lattice constant, see Fig. 1(b). The corresponding reciprocal lattice vectors are

$$\mathbf{G}_{mn} = m\mathbf{b}_1 + n\mathbf{b}_2, \tag{2}$$

where m, n are integers, $\mathbf{b}_1 = \beta_0(1/2, -\sqrt{3}/2)$ and $\mathbf{b}_2 = \beta_0(1/2, \sqrt{3}/2)$ are the primitive reciprocal lattice vectors, and $\beta_0 = 4\pi/(\sqrt{3}a)$. The six fundamental in-plane wavevectors with magnitude $|G_{mn}| = \beta_0$ correspond to $(m, n) = (1, 0), (-1, 0), (0, 1), (0, -1), (1, 1)$, and $(-1, -1)$, and are denoted as R_1, S_1, R_2, S_2, R_3, and S_3, respectively, following the convention of [8]. These wavevectors define the first-order in-plane waves used in the coupled-wave theory and are illustrated in Fig. 1(c). The hexagonal lattice is chosen for its high in-plane symmetry and large two-dimensional coupling coefficients [3,23], which enhance in-plane feedback and facilitate low-threshold two-dimensional lasing. While the modeling in this work focuses on this specific structure, the simulation frameworks developed in the following sections are general and can be applied to other photonic-crystal geometries, including square lattices.

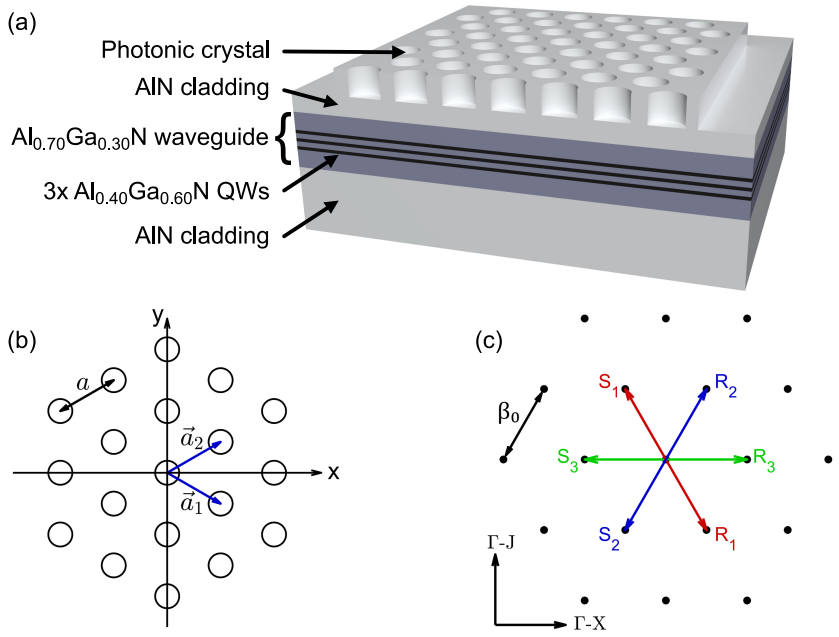

Fig. 1. (a) Schematic of the UV-C PCSEL structure with a hexagonal photonic crystal etched into the top AlN cladding layer. (b) Real-space diagram of the hexagonal lattice with primitive lattice vectors $\vec{a}_1$ and $\vec{a}_2$, where a is the lattice constant. (c) Corresponding reciprocal lattice showing the six second-order Γ-point wavevectors R_1, S_1,. . . , S_3, used in coupled-wave theory. These wavevectors define the dominant in-plane components of the lasing mode and form the basis for the bandstructure models discussed in this work. The high-symmetry directions $\Gamma - X$ and $\Gamma - J$ in reciprocal space are indicated.

2.2. *Structural parameters and refractive index modeling*

The lattice constant is $a = 136$ nm, corresponding to a target lasing wavelength of approximately 275 nm. Hole fill-factors, i.e. hole to unit cell area, between 10% and 25% are considered in

Optics EXPRESS

the simulations. For a given fill-factor, the average refractive index in the photonic crystal layer is obtained using the effective medium approximation, $n_{avg} = \sqrt{FFn_{air}^2 + (1-FF)n_{AlN}^2}$, where FF is the fill-factor, $n_{air} = 1$ and $n_{AlN} = 2.28$. The vertical layer structure is summarized in Table 1. The device consists of a vertically symmetric AlN/AlGaN waveguide stack, with three AlGaN quantum wells in the active region. The design of the active region and waveguide was developed in conjunction with active regions for UV-C VCSELs and in-plane laser diodes [5,24]. For modeling purposes, the active region is assumed to have the same refractive index as the surrounding waveguide layers when pumped to transparency, since the carrier-induced refractive index change largely removes the index contrast under these conditions. All simulations use refractive indices evaluated at the design wavelength of 275 nm.

Table 1. Layer structure and refractive indices used in simulations at λ = 275 nm.

Layer	Thickness [nm]	Refractive index
Photonic crystal (AlN/air)	300	n_{avg}
Cladding (AlN)	20	2.280
Waveguide ($Al_{70}Ga_{30}N$) and active region ($Al_{40}Ga_{60}N$)	76	2.458
Cladding (AlN)	1000	2.280

3. Infinite PCSEL dispersion models

In this section, we present two models used to describe the infinite PCSEL structure: the three-dimensional coupled-wave theory (CWT) developed by Liang et al. [8], and the guided-mode expansion (GME) method [9]. These models provide the modal inputs to the k-space weighted loss estimation (kSWLE) framework introduced later in Section 5. While CWT also forms the basis of the finite-CWT method, GME includes a more rigorous physical treatment of the bandstructure.

3.1. Coupled wave theory

The CWT approach expands the electromagnetic field inside the photonic crystal using six dominant in-plane waves R_1 to S_3, as defined in Fig. 1(c). They share the same vertical mode profile $E_{\mathbf{G}}^{\text{guided}}(z)$, which is taken from the fundamental mode of the effective waveguide [25]. The total field of any one of the six modes $\mu \in \{A, B_1, B_2, C, D_1, D_2\}$ can be written as

$$\mathbf{E}_{\mathbf{k}}^{\mu}(\mathbf{r}) = \sum_{\mathbf{G}\in\mathbf{G}^{\text{fund}}} c_{\mathbf{G},\mathbf{k}}^{\mu} e^{i\mathbf{r}\cdot\mathbf{k}}\, \mathbf{E}_{\mathbf{G}}^{\text{guided}}(z)\, e^{i\mathbf{r}\cdot\mathbf{G}} + \text{Higher order}, \tag{3}$$

where $c_{\mathbf{G},\mathbf{k}}^{\mu}$ are the in-plane mode amplitudes and G^{fund} denotes the six fundamental wavevectors fulfilling $|\mathbf{G}_{mn}| = \beta_0$. The coupling between these first-order waves is induced by the periodic modulation of the refractive index. The corresponding coupling coefficients are determined by the Fourier components of the spatial dependency of the permittivity $\varepsilon(\mathbf{r}) = n^2(\mathbf{r})$, where $n(\mathbf{r})$ is the refractive index, and by the modal overlap between the interacting waves. These coefficients are organized into a 6×6 coupling matrix C_f, which reflects the in-plane feedback in the hexagonal structure. In addition, a vertical loss term C_r accounts for vertical outcoupling losses introduced through perturbation theory, and a perturbative term C_h accounts for the influence of higher-order waves generated by the scattering from the first-order waves [8]. Finally, a diagonal term $d_{k0,mn}$ represents the detuning of the individual basic wavevectors from the second-order Γ-point. Taking these contributions together, and inserting the ansatz in Eq. (3) into Maxwell's equations, the coupled eigenvalue problem describing the optical modes in the

Optics EXPRESS

PCSEL of infinite extent is obtained as

$$(d_{k0,mn} + C_f + C_r + C_h)\begin{bmatrix} R_1 \\ S_1 \\ R_2 \\ S_2 \\ R_3 \\ S_3 \end{bmatrix} = (\delta + i\frac{\alpha}{2})\begin{bmatrix} R_1 \\ S_1 \\ R_2 \\ S_2 \\ R_3 \\ S_3 \end{bmatrix}, \tag{4}$$

where δ denotes the spatial frequency detuning from the Bragg condition, and α represents the vertical loss. The explicit 6×6 forms of the matrices $d_{k0,mn}$, C_f, C_r, and C_h are given by Liang *et al.* [8]. The physical mode frequency ω is related to δ through the relation

$$\omega = c\frac{\delta + \beta_0}{n_{\text{eff}}}, \tag{5}$$

where n_{eff} is the effective index of the guided mode and β_0 is the corresponding propagation constant at the Bragg resonance.

3.2. Guided mode expansion

The optical modes in a photonic crystal slab can also be analyzed using the GME method, which solves Maxwell's equations in a periodic multilayer slab by expanding the electromagnetic fields in a bases of guided modes of an effective homogeneous waveguide [9]. The eigenvalue problem for the magnetic field is

$$\nabla \times \left(\frac{1}{\varepsilon(\mathbf{r})}\nabla \times \mathbf{H}(\mathbf{r})\right) = (\omega/c)^2\mathbf{H}(\mathbf{r}), \tag{6}$$

where $\mathbf{H}(\mathbf{r})$ is the magnetic field, $\varepsilon(\mathbf{r})$ is the position-dependent dielectric function, ω is the angular frequency, and c is the speed of light in vacuum.

In this method, the in-plane periodicity of the structure is treated using Bloch's theorem, and the fields are expanded as

$$\mathbf{H}^{\mu}_{\mathbf{k}}(\mathbf{r}) = \sum_{\mathbf{G},\upsilon} c^{\mu}_{\mathbf{G},\upsilon,\mathbf{k}}\, \mathbf{H}^{\text{guided}}_{\mathbf{k}+\mathbf{G},\upsilon}(z)\, e^{i(\mathbf{k}+\mathbf{G})\cdot\mathbf{r}}, \tag{7}$$

where $\mathbf{k}$ is the in-plane Bloch wavevector, $\mathbf{G}$ are the reciprocal lattice vectors, and υ indexes the guided modes of an effective homogeneous slab waveguide. The functions $\mathbf{H}^{\text{guided}}_{\mathbf{k}+\mathbf{G},\upsilon}(z)$ are the vertical profiles of these modes, and $c^{\mu}_{\mathbf{G},\upsilon,\mathbf{k}}$ are the expansion coefficients.

The method assumes that the dielectric structure can be approximated by a homogeneous slab in vertical direction for the computation of the guided modes. The photonic crystal modulation is treated perturbatively, and the basis set is truncated at a chosen maximum $|\mathbf{k} + \mathbf{G}|$. Vertical losses are introduced by perturbative coupling to radiation modes, and the imaginary part of the frequency is computed using time-dependent perturbation theory.

In contrast to coupled-wave theory, which expands the fields in terms of six in-plane wavevectors in the case of a hexagonal lattice, GME uses a large number of in-plane guided modes and reciprocal vectors. Note that GME is capable of simulating higher order vertical modes, e.g. those caused by the substrate or thick cladding layers. However, in this paper we used only the fundamental vertical mode ($\upsilon = 1$) to be compatible with standard literature. In this work, we only consider TE-like modes for compatibility with the implementation of CWT in [7] and because optical gain is higher for TE polarization for the investigated UV-C PCSEL structures, as

Optics EXPRESS

shown theoretically [26] and experimentally [27] for similar AlGaN active regions. While there are implementations of GME which account for polarization mixing, such effects are neglected in this comparison [9], to ensure a fair TE-only comparison with the CWT model, which does not include polarization mixing. The same vertical slab and refractive index profile are used for both methods to ensure consistency.

3.3. Photonic band structure, group velocity and vertical loss

We now compare the photonic properties derived from the CWT and GME methods, focusing on how their respective approximations influence computed eigenfrequencies, group velocities, and vertical losses. Before doing so, it is helpful to summarize the modeling assumptions and features of the two methods (see Table 2), since these choices directly influence the bandstructure, group velocity, and vertical loss predictions discussed below. As previously discussed, CWT uses a minimal set of six plane waves and treats higher-order effects perturbatively, whereas GME includes a much larger reciprocal-space basis and solves the full-wave problem. These distinctions affect not only the calculated bandstructures but also derived quantities such as group velocity and vertical radiation loss. In this section, we evaluate and compare results from both methods while varying the number of included wavevectors.

Table 2. Comparison of modeling assumptions and features of CWT and GME.

Feature	CWT	GME
Field expanded in	First order in-plane waves of **E** field (R_1–S_3)	Guided-mode basis for **H** field in slab
Vertical field profile	Fixed single profile $\Theta_0(z)$ from TMM	Full set of guided modes (fundamental TE only used here)
In-plane wavevectors	6 first-order wavevectors + higher-order treated perturbatively	Arbitrary number of reciprocal vectors **G** (plane-wave basis)
Permittivity expansion	$\varepsilon(\mathbf{r})$ expanded directly	$1/\varepsilon(\mathbf{r})$ inside the Hermitian operator
Vertical loss	Included directly in the eigenvalue problem via radiation coupling terms, C_r	Computed after solving the eigenvalue problem using time-dependent perturbation theory
Numerical truncation	6 first-order waves always; higher-order waves are treated as a perturbation and expressed in terms of first-order waves	Allows inclusion of any number of basis functions

Figure 2 shows the calculated band structures using both methods for two cases: (a) when a minimal set of six in-plane wavevectors ($N_G = 6$) is used, and (b) when a more extended basis of 81 wavevectors is included ($N_G = 81$). When $N_G = 6$, the band structures obtained from CWT and GME agree closely across most bands near the Γ-point, especially for A, B_1, B_2 and C modes. A larger discrepancy is observed for the D bands, where the GME solutions exhibit a minimum at wavelengths shorter than the CWT counterparts. When $N_G = 81$ is used, the deviation between the two methods becomes more pronounced and the separation of the bands are larger for the GME method as compared to CWT. This reflects the more complete basis set used in GME and its ability to account for modal interactions beyond the basic six-wave approximation. The change in the band structure for GME in the two cases is large, and the convergence analysis for these two methods shown in Fig. 3(a) shows that both methods are well converged for $N_G = 81$.

In contrast, CWT yields a nearly constant mode position across all bands regardless of N_G>6, showing that the impact of higher-order components, which are treated as a perturbation, has a small impact. It is interesting to note that for CWT, the degeneracy of the B and D modes is lifted for small N_G, as can be seen in Fig. 3(a). For example, the two gray crosses for D_1 and D_2 are slightly shifted in wavelength. This is due to the fact that the higher-order perturbative terms, C_{2D}, are calculated for wavevectors lying in a rhombus which lacks the hexagonal symmetry [8].

Optics EXPRESS

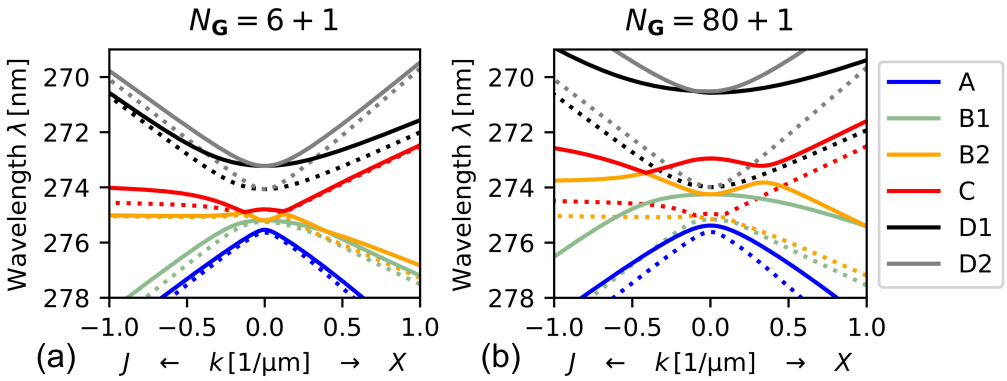

Fig. 2. Dispersion relations $\lambda(k)$ near the Γ-point computed using GME (solid lines) and CWT (dotted lines). Results are shown for two different basis sizes: (a) a minimal set of six wavevectors ($N_G = 6$), and (b) an extended basis including 80 wavevectors ($N_\mathbf{G} = 80$), plus the radiative mode. The CWT model includes only six first-order in-plane plane waves in the field expansion; higher-order wavevector effects are included perturbatively (see Section 3.1).

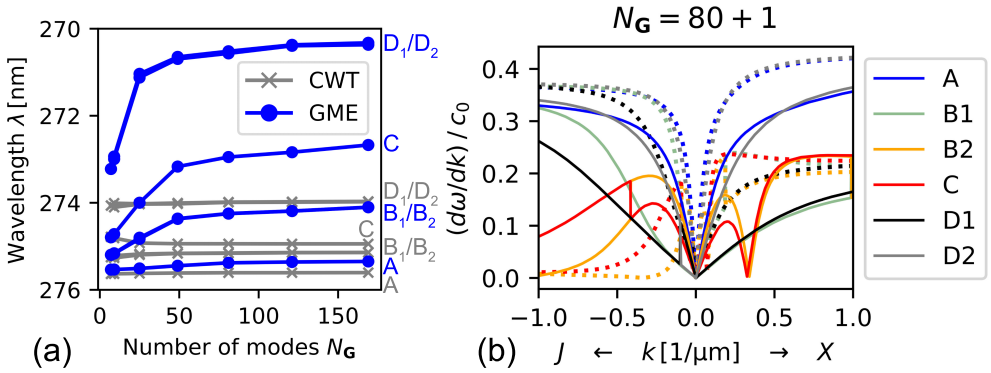

Fig. 3. (a) Modal wavelengths at the Γ-point for the six lowest-order modes, computed using CWT (gray crosses) and GME (blue circles), as a function of the number of in-plane components or modes used in the expansion. (b) Group velocity dispersion $\partial\omega/\partial k$, normalized to the speed of light c, along the $\Gamma - J$ and $\Gamma - X$ directions for each mode, computed using GME (solid lines) and CWT (dotted lines) for $N_\mathbf{G} = 81$. CWT results include only six first-order waves, while higher-order effects are incorporated perturbatively (see Section 3.1).

This effect can be eliminated by calculating the higher-order waves for wavevectors lying within a circle. However, in practice it does not make a big difference as it is easy to include many waves in the CWT formulation without sacrificing computation time.

From the bandstructure, the group velocity can be extracted as the gradient of the dispersion relation. Figure 3(b) shows the group velocity along the $\Gamma - X$ and $\Gamma - J$ directions using $N_G = 81$. Since group velocity is proportional to the gradient of the bandstructure, the differences observed in Fig. 2(b) between the CWT and GME models result in corresponding deviations in the group velocity. This quantity is directly related to lateral energy transport and thus plays a critical role in determining lateral losses, as discussed in Section 5.

The group velocity is zero not only at the Γ-point, but also at maxima or minima of the dispersion at avoided crossings. This is the case at $k \approx 0.33\ \mu\text{m}^{-1}$ in $\Gamma - X$ direction in Fig. 2(b)

Optics EXPRESS

for GME, where the B_2 and C branches approach without touching, forcing their curvature to change sign and the group velocity to vanish as shown in Fig. 3(b). By contrast, when the branches touch, the group velocity becomes undetermined. These avoided crossings occur at Dirac points in k-plane [28], and the individual branches of the dispersion are continuous in the vicinity of the crossing point. Therefore we label the branches according to the respective leaf. This has the consequence that the group velocity is discontinuous at those points, as observed in Fig. 3(b) at $k \approx -0.42$ μm^{-1} in $\Gamma - J$ direction for GME. Also note that the modal composition changes character from B_2 to C and vice versa, when crossing the Dirac point along this $\Gamma - J$ direction. On a path encircling the singularity, this change is gradual and continuous, justifying our choice to label the branches.

The vertical losses for both methods are shown in Fig. 4. As expected, the vertical loss of the A, B_1, B_2 and C modes vanishes at the Γ point due to symmetry of the electric field around a photonic crystal hole. However, outside the Γ-point, significant differences emerge. In the minimal $N_G = 6$ case, both methods predict similar qualitative features, but with noticeable quantitative discrepancies in peak loss values and positions. With $N_G = 81$, GME predicts much sharper features and stronger dependence on in-plane momentum. In contrast, CWT continues to yield smoother loss trends, reflecting its inability to fully resolve the high-order scattering channels captured by GME.

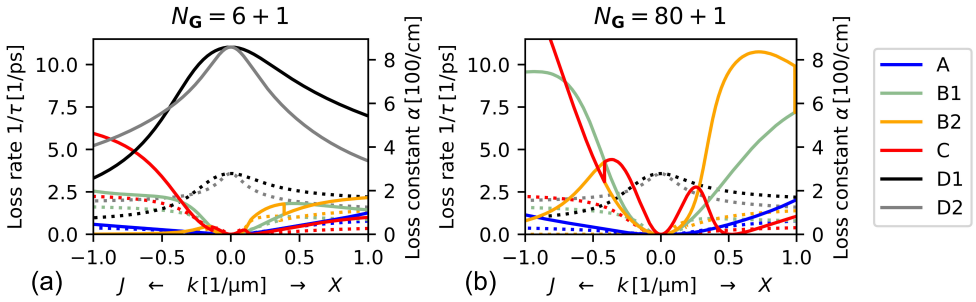

Fig. 4. Vertical loss rates $\alpha(k)$ obtained using GME (solid lines) and CWT (dotted lines) along $\Gamma - J$ and $\Gamma - X$ directions in reciprocal space. Results are shown for two different basis sizes: (a) a minimal set of six wavevectors ($N_G = 6$), and (b) an extended basis including 80 wavevectors ($N_G = 80$), plus the radiative mode. In the CWT model, the field expansion includes only the six first-order in-plane waves; higher-order wavevector contributions are treated perturbatively via the C_h coupling matrix (see Section 3.1). Note that the D modes for the GME lie outside of the shown region in (b).

Although the CWT model provides an approximate description of PCSELs, it has been shown to agree well with experimental results for hexagonal lattices [8]. This is somewhat surprising, given that the method only includes six in-plane wavevectors and treats higher-order interactions perturbatively. In contrast, GME allows for the coupling between an arbitrary number of reciprocal lattice vectors, enabling a more complete representation of the mode structure and associated losses. Nonetheless, the predictive accuracy of CWT remains high. One possible reason is that a deviation of the photonic crystal from the ideal geometry, which is inherent to fabricated devices, tends to suppress coupling to higher-order wavevectors, an effect not explicitly captured in the idealized models but one that naturally limits their influence in practice. Consequently, the coupling strength to the photonic crystal may be weaker than assumed, due to shallow etch depths, tapered holes, partially filled holes, or a spatial variation of the hole diameter, all of which can weaken higher-order coupling. Another potential explanation is polarization mixing, which is not included in our CWT formulation. When TM polarization is also included in GME, six additional bands appear near the original TE modes, and the resulting 12 bands are no

Optics EXPRESS

longer purely TE or TM. This mixing shifts the overall bandstructure, particularly the nominally TM-like D bands, closer to the TE-like modes predicted by CWT, making the dispersion more similar to the uncoupled TE bandstructure assumed in CWT. As a result, although CWT models only six in-plane components and a single polarization, it may still capture the dominant lasing modes in real devices, where structural disorder and fabrication imperfections limit the excitation of higher-order and polarization mixed components.

The quantitative differences observed here between CWT and GME predictions suggest that the choice of a bandstructure model can significantly affect lateral and vertical loss estimates. This motivates the development of a general framework that enables loss estimation based on arbitrary infinite-structure band information, a topic discussed in Section 5 with the introduction of the k-space weighted loss estimation (kSWLE) model.

4. Finite-size calculations and mode decomposition

To account for finite-size effects in PCSELs, the CWT formalism described in the previous section can be extended by incorporating the spatial variation of the lateral field through spatial derivatives of the first-order wave amplitudes. This results in a generalized eigenvalue problem defined on a hexagonal grid, as discussed in Ref. [8]. For band-edge modes ($k = 0$), the discretized form leads to the generalized eigenvalue equation

$$(\delta + i\frac{\alpha_{tot}}{2})\begin{bmatrix} R_1(\mathbf{r}) \\ S_1(\mathbf{r}) \\ R_2(\mathbf{r}) \\ S_2(\mathbf{r}) \\ R_3(\mathbf{r}) \\ S_3(\mathbf{r}) \end{bmatrix} = \mathbf{C}\begin{bmatrix} R_1(\mathbf{r}) \\ S_1(\mathbf{r}) \\ R_2(\mathbf{r}) \\ S_2(\mathbf{r}) \\ R_3(\mathbf{r}) \\ S_3(\mathbf{r}) \end{bmatrix} + i\begin{bmatrix} \frac{1}{2}\partial R_1/\partial x - \frac{\sqrt{3}}{2}\partial R_1/\partial y \\ -\frac{1}{2}\partial S_1/\partial x + \frac{\sqrt{3}}{2}\partial S_1/\partial y \\ \frac{1}{2}\partial R_2/\partial x + \frac{\sqrt{3}}{2}\partial R_2/\partial y \\ -\frac{1}{2}\partial S_2/\partial x - \frac{\sqrt{3}}{2}\partial S_2/\partial y \\ \partial R_3/\partial x \\ -\partial S_3/\partial x \end{bmatrix}. \tag{8}$$

Here, the 6×6 matrix $\mathbf{C} = d_{k0,mn} + C_f + C_r + C_h$ is the same as in Eq. (4) and contains the coupling coefficients between these waves and incorporates vertical radiation losses. The real part of the eigenvalue corresponds to the frequency detuning δ from the Bragg condition, and the imaginary part α_{tot} represents the modal loss, including both vertical loss and lateral leakage. This framework can be used to calculate field profiles, far-field patterns, and lasing thresholds, and has been shown to agree well with experimental observations [8]. In Section S1 of the Supplement 1, we show how the computed total loss can be decomposed into a vertical and lateral loss part.

To understand how the resulting finite-size solutions relate to the modes of an ideal infinite PCSEL, we perform a mode decomposition. The spatially varying first-order wave amplitudes ($R_1(x, y)$–$S_3(x, y)$) of the finite structure are at first Fourier transformed to obtain their spectral components in reciprocal space. For each wavevector k, the corresponding six-component Fourier vector is then expanded in the basis of the infinite-system eigenvectors at that k-point. This yields the contribution of each infinite-system band (A, B_1, B_2, C, D_1, D_2) to the finite structure's fields. A more detailed description of this process is provided in Section S2 of the Supplement 1. For illustration, we focus on the C-mode, which is identified as the lowest-loss mode in the finite-CWT model for a fill factor of 15%. Figure 5 shows the mode decomposition of the C-mode for a finite PCSEL with a radius of $L = 100$ μm. It is seen that the C-mode of the finite system has a predominant contribution from the C-mode of the infinite system. Figure 6(a) shows the corresponding 1D intensity profile in the vicinity of the Γ-point, which matches closely with a Gaussian distribution with standard deviation $\sigma_k = \pi/(2L)$.

Optics EXPRESS

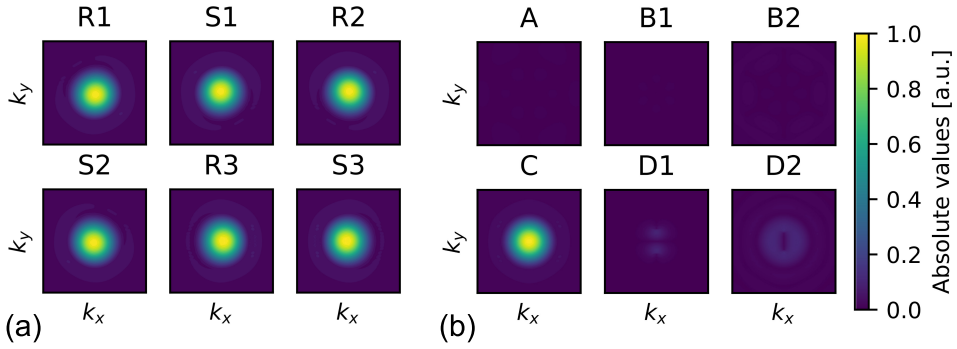

Fig. 5. (a) Absolute values of the 2D discrete Fourier transforms of the six in-plane field components R_1 through S_3, extracted from the finite-size C-mode solution for $L = 100$ μm and fill-factor $FF = 15\%$. This shows the raw spectral content of the finite mode in reciprocal space. (b) Modal decomposition showing contributions from the six infinite-system bands ($A - D_2$), obtained by projecting the Fourier-transformed finite field in (a) onto the infinite-system eigenvectors at each **k**-point. The decomposition shows that the finite C-mode is dominated by the infinite C-band with only weak mixing from other bands.

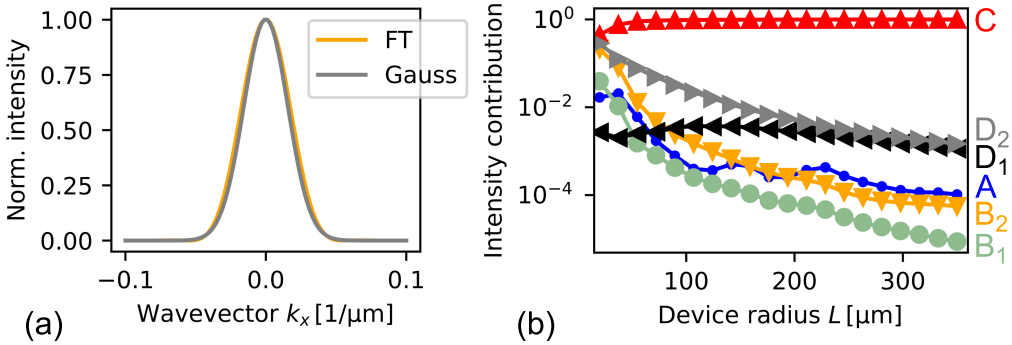

Fig. 6. (a) Normalized intensity distribution of the finite C-mode along $k_y = 0$, obtained by Fourier transforming (FT) the real-space field from finite-CWT simulations for a device with a radius $L = 100$ μm and fill factor $FF = 15\%$ (orange). The overlaid curve (gray) shows a Gaussian fit with standard deviation $\sigma_k = \pi/(2L)$, which is used to approximate the spectral weighting in the kSWLE model. (b) Modal contributions from each of the six infinite-system bands ($A - D_2$) to the finite C-mode, extracted via mode decomposition as a function of device radius L at a fixed fill factor $FF = 15\%$.

Optics EXPRESS

To explore how this modal composition evolves with device size, we repeat the decomposition for a varying lateral radius L (used to be consistent with [8]), as shown in the example for the finite-sized C-mode in Fig. 6(b). For large devices, the optical mode is spatially broad, while its k-space distribution is narrow, leading to strong overlap with a single infinite-system band. In contrast, for small devices, the field varies more rapidly, resulting in broader k-space components and significant contributions from multiple bands. This behavior can be understood from the finite-CWT formulation: as the device size increases, the spatial derivatives in Eq. (8) become negligible ($\partial/\partial x \sim 1/L$), and the coupling term involving the $\mathbf{C}$ matrix dominates. Consequently, the coupling between components resembles that of the infinite system. In smaller systems, however, the derivative term becomes significant, causing stronger perturbations and greater deviation from the ideal infinite-system mode structure. As a result, the mode can no longer be uniquely associated with a single infinite-system band, making its classification ambiguous. In some cases, no clear C-like mode exists at all, emphasizing the importance of caution when extrapolating band-based intuition to strongly confined systems.

5. Loss estimation for finite devices using dispersion

Optical modes in finite-size PCSELs are not confined to the Γ-point but span a distribution of in-plane wavevectors due to diffraction, as shown in Section 4. This motivates a dispersion-based approach in which modal losses are estimated by weighting the vertical loss and group velocity of the infinite structure across this $\mathbf{k}$-space distribution. An example of the underlying band dispersion, vertical loss, and group velocity surfaces, computed using CWT, is shown in Fig. 7. In this section, we formalize this concept by introducing the kSWLE framework; a semi-analytical method that enables loss evaluation based on the infinite-structure bandstructure alone. We then apply kSWLE to both CWT and GME input data to evaluate its performance and compare it with results from finite-CWT simulations.

5.1. Framework of k-space weighted loss estimation (kSWLE)

The k-space weighted loss estimation (kSWLE) model provides a semi-analytical way to estimate modal losses without solving the full field distribution in a finite geometry. Because the real-space mode profile and its reciprocal-space representation are related through the Fourier transform, the in-plane optical mode of a sufficiently large PCSEL becomes naturally localized near the Γ-point in reciprocal space. In Section 4, we showed using finite-CWT simulations that the fundamental mode possesses a Gaussian-like spatial envelope, and correspondingly a Gaussian-shaped $\mathbf{k}$-space intensity profile $I(\mathbf{k})$, which is well approximated by

$$I(\mathbf{k}) = \frac{1}{2\pi\sigma_k^2} \exp\left(-\frac{|\mathbf{k}|^2}{2\sigma_k^2}\right), \quad \sigma_k = \pi/(2L), \tag{9}$$

where L is the PCSEL radius. While the Gaussian approximation in Eq. (9) is well-justified for moderately large apertures, it becomes less accurate when the device radius is small or when the bandstructure contains strongly overlapping modes. In such cases, the finite-size lasing mode may draw significant spectral weight from multiple bands, violating the assumption that it can be represented by a single Gaussian envelope in $\mathbf{k}$-space. As shown in the mode decomposition analysis in Section S3 of the Supplement 1, these effects can lead to spectral shapes and band mixing that are not captured by the Gaussian approximation. Under such conditions, kSWLE may not provide accurate loss estimates. A quantitative analysis in Section S3.1 shows that, for the device considered here, the Gaussian approximation is accurate to within 3% of the finite-size C-mode for radii $L \geq 60$ μm.

When the optical mode in reciprocal space can be approximated by a single Gaussian distribution, the total vertical loss α_{vert} can be estimated as a weighted average of the vertical loss

Optics EXPRESS

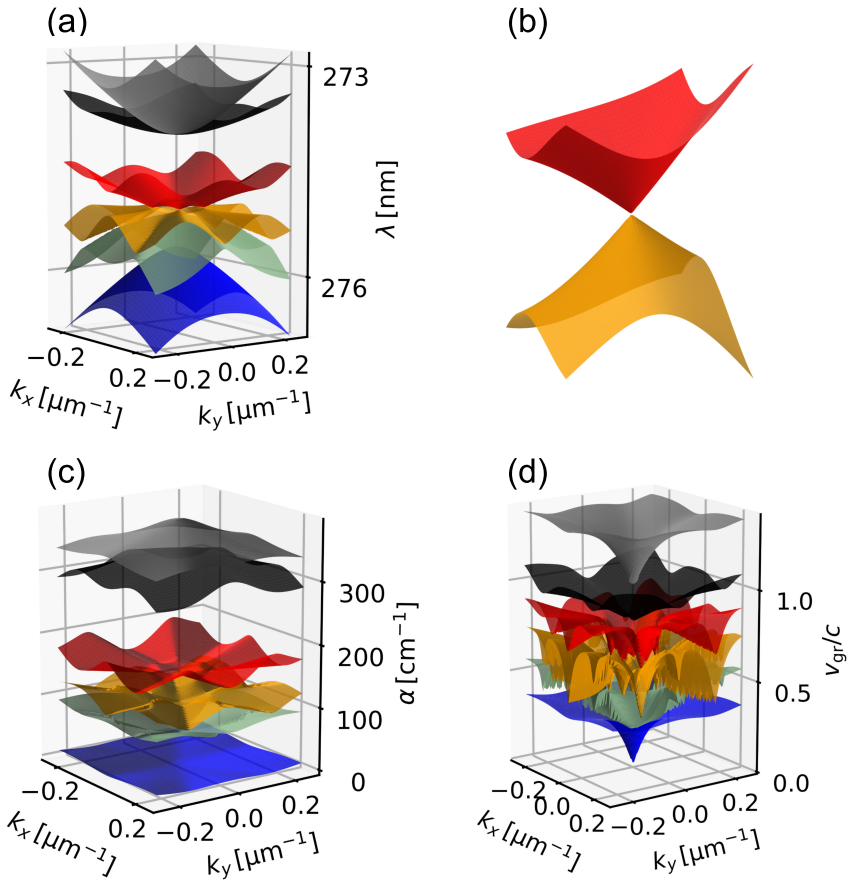

Fig. 7. Two-dimensional maps of the six fundamental PCSEL modes computed using the infinite-CWT method for a fill factor of 15%. (a) Wavelength dispersion surfaces $\lambda(k_x, k_y)$, (b) dispersion in the vicinity of a Dirac-like crossing point at $\{k_x \approx 0.078\ \mu\text{m}^{-1}; k_y \approx 0.043\ \mu\text{m}^{-1}\}$ from (a), (c) vertical loss rate $\alpha(k_x, k_y)$, and (d) group velocity normalized to the speed of light, $v_{gr}(k_x, k_y)/c$. For visual clarity, the surfaces in (c) and (d) are vertically offset by $50\,\text{cm}^{-1}$ and $0.2c$, respectively, between subsequent branches.

rate $\text{Im}[\omega(\mathbf{k})]$ obtained from the infinite system, as shown in Fig. 7(c)

$$\alpha_{\text{vert}} = \frac{1}{v_{\text{ph}}} \int I(\mathbf{k}) 2\text{Im}[\omega(\mathbf{k})] dk_x dk_y, \tag{10}$$

where the loss rate is converted to a spatial decay rate using the phase velocity of the guided mode $v_{ph} = c_0/n_{\text{eff}}$, and n_{eff} is the effective index of the mode. This captures the fact that finite-size modes contain components away from the Γ-point, where vertical outcoupling is nonzero, even for antisymmetric modes (A, B_1, B_2 and C) that are symmetry protected at $k = 0$.

The lateral loss α_{lat} is similarly estimated by assuming that energy escapes from the device over a characteristic time scale determined by the group velocity $v_{\text{gr}}(\mathbf{k}) = |\nabla_k \omega(\mathbf{k})|$, as shown in Fig. 7(d), and the device radius. Under this assumption, the lateral loss is

$$\alpha_{\text{lat}} = \frac{1}{v_{\text{ph}}} \int I(\mathbf{k}) \frac{|\nabla_k \omega(\mathbf{k})|}{2L} dk_x dk_y. \tag{11}$$

Optics EXPRESS

The underlying idea behind the approximation originates from the fact that the term $2L/|v_{gr}|$ constitutes a characteristic time scale for a wave-packet to transverse the diameter of the devices. Therefore, the inverse of this time constant is assumed as loss rate. The choice of $2L$ for the characteristic length scale is somewhat heuristic, as the mode is not homogeneous across the PCSEL area. However, this length only enters Eq. (11) as an overall prefactor: replacing $2L$ with, for example, L or $1.5L$ would uniformly rescale α_{lat} without modifying its dependence on device size or the trends discussed in Section 5.3.

Using the vertical and lateral loss components defined in Eqs. (10) and (11), the total modal loss is then

$$\alpha_{tot} = \alpha_{vert} + \alpha_{lat}. \tag{12}$$

The kSWLE approach retains physical interpretation of modal losses in terms of band curvature and outcoupling strength, quantities which are readily accessible from dispersion simulations of the infinite PCSEL.

5.2. Parabolic-band approximation

In the large-radius limit, the mode becomes strongly localized in k-space near the Γ-point, where both the band dispersion and the vertical loss can be approximated as parabolic

$$\mathrm{Re}[\omega(\mathbf{k})] \approx \omega_0 + \frac{b}{2}k^2, \quad \mathrm{Im}[\omega(\mathbf{k})] \approx \gamma_0 + \frac{l}{2}k^2, \tag{13}$$

where $k = |\mathbf{k}|$. The constant b describes the curvature of the real part of the band dispersion, while l characterizes the curvature of the imaginary part, which corresponds to the vertical loss rate. These parameters are obtained from the infinite-system bandstructure near the Γ-point. The term γ_0 accounts for vertical losses at k = 0; it is zero for non-radiative $A - C$ modes, but positive for D modes, which are radiative at the Γ-point. Using the parabolic approximation of the dispersion and vertical loss in Eq. (13), together with the Gaussian k-space mode profile in Eq. (9), the integrals in Eqs. (10) and (11) can be evaluated analytically. This yields closed-form scaling laws for the lateral and vertical loss contributions

$$\alpha_{lat} \propto bL^{-2}, \quad \alpha_{vert} \propto lL^{-2}. \tag{14}$$

This L^{-2} scaling behavior is confirmed in our numerical results, as shown in Fig. 8(a), and provides intuitive understanding of how confinement influences losses: both vertical and lateral losses decreases with increasing aperture size, as the optical mode becomes more localized in k-space. These expressions provide intuitive understanding of how the modal losses evolve with device size, particularly in the large-area limit where the Gaussian envelope assumption is well justified.

5.3. Scaling behavior of finite-CWT, kSWLE:CWT, and kSWLE:GME

We apply the kSWLE framework using dispersion data from both CWT (kSWLE:CWT) and GME (kSWLE:GME), and compare the results with finite-CWT. This comparison allows us to assess the influence of both the infinite-structure model and the evaluation method on the predicted losses. Figure 8 shows vertical, lateral, and total modal losses as a function of device radius for the six fundamental bands.

For vertical losses, see Fig. 8(a), the kSWLE:CWT and kSWLE:GME models yield qualitatively similar trends for the B-, C-, and D-modes (except for the A-mode at large device radii) but differ quantitatively, especially for the D modes, which exhibit stronger radiation in GME due to this method's more complete treatment of radiative channels. The B and C modes both follow the expected trend of L^{-2}, consistent with the parabolic-band approximation in Eq. (14). Compared with finite-CWT, both kSWLE approaches reproduce similar scaling behavior but

Optics EXPRESS

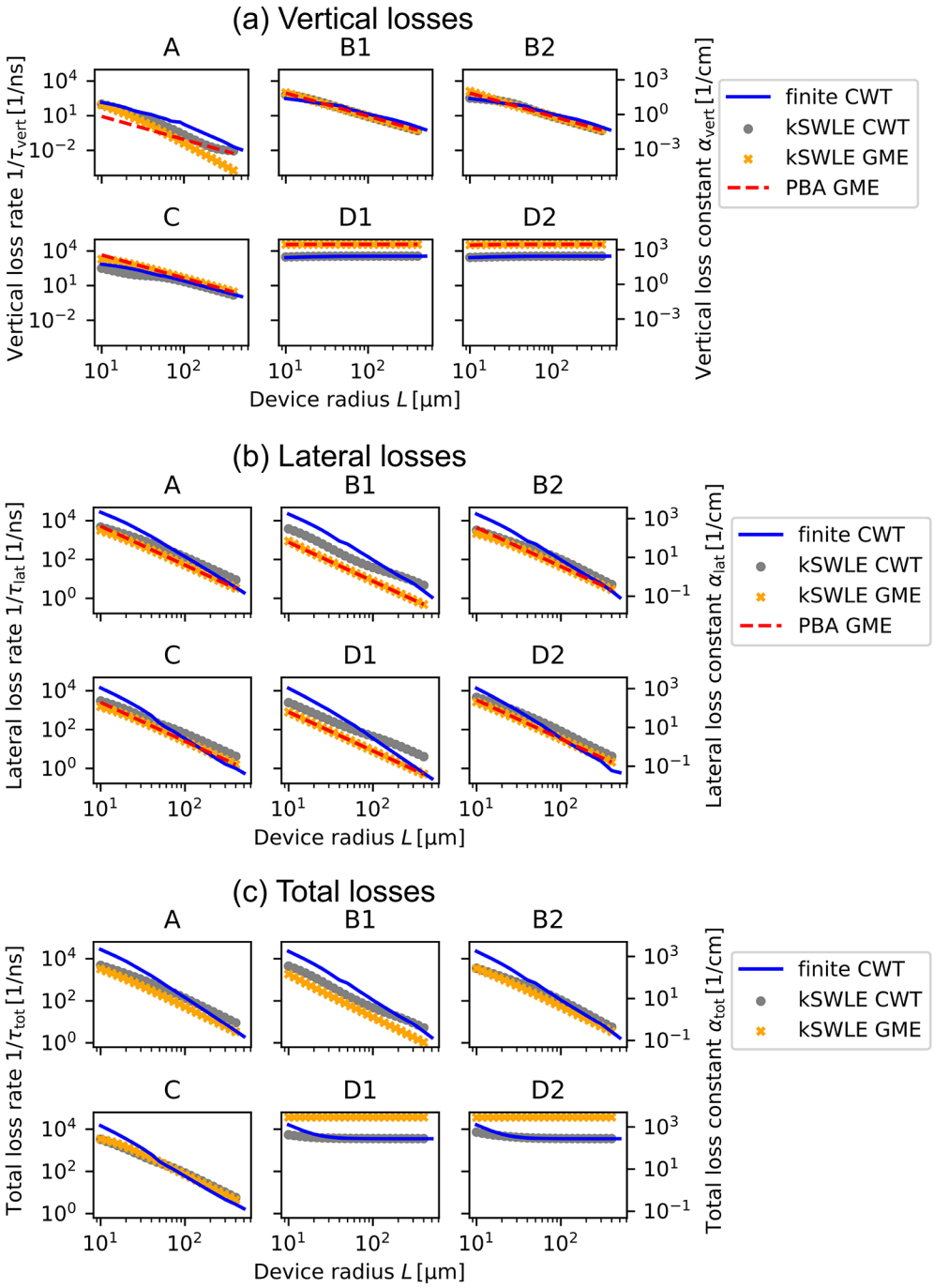

Fig. 8. Calculated (a) vertical, (b) lateral, and (c) total losses for the A, B_1, B_2, C, D_1, and D_2 modes as a function of device radius L, for a fill factor of $FF = 15\%$. Each subplot compares finite-CWT results (blue line) with kSWLE predictions based on CWT (gray circles) and GME (orange crosses), as well as the parabolic band approximation (PBA) based on GME (red dashed line). The double-logarithmic scale reveals the power-law scaling of radiative and lateral losses with device radius and enables comparison of trends across a wide range of radii.

Optics EXPRESS

yield systematically different absolute loss values, which reflects differences in the loss evaluation method. Interestingly, the A-mode shows a significant deviation from this behavior: both kSWLE:CWT and kSWLE:GME predict that its vertical loss, $\mathrm{Im}[\omega(\mathbf{k})]$, scales approximately as k^4 near $k = 0$, rather than the assumed k^2. This leads to a stronger-than-expected scaling of α_{vert} with device size, approximately L^{-4}, deviating from the L^{-2} trend implied by Eq. (14). Although we do not derive this behavior analytically, it can be interpreted based on symmetry. The hexapole symmetry of the A-mode [8] appears to suppress first-order coupling between the in-plane electric field and the radiative plane waves, resulting in a k^2 dependence of the coupling amplitude. Since the radiated power is proportional to the square of this overlap, the resulting loss scales as $\mathrm{Im}[\omega(\mathbf{k})] \propto k^4$. In contrast, the B and C modes, which have dipole- and monopole-like symmetry, allow for nonzero first-order overlap, yielding $\mathrm{Im}[\omega(\mathbf{k})] \propto k^2$.

For lateral losses, see Fig. 8(b), both models again predict similar L^{-2} scaling as obtained with the parabolic band approximation (PBA), but with different prefactors. These discrepancies reflect differences in band curvature and group velocity dispersion between the CWT and GME calculations. Since lateral losses in kSWLE are sensitive to the slope of the band curvature near Γ, even modest differences in curvature lead to different estimates. The D modes again show the largest differences, consistent with the deviations observed in their group velocities in Fig. 2. For lateral losses, see Fig. 8(b), finite-CWT predicts a steeper scaling with radius, approximately $L^{-2.4}$, while both kSWLE:CWT and kSWLE:GME predict L^{-2} decay, consistent with the parabolic-band approximation. The steeper decay in finite-CWT likely reflects a fundamental difference in how lateral leakage is modeled. In kSWLE, lateral losses are estimated by assuming that energy escapes from a spatially localized mode at a constant group velocity, following a wave-packet-like picture. In contrast, finite-CWT treats lateral losses as steady-state outcoupling, where the leakage depends on the modal amplitudes at the device boundary. These different assumptions lead to distinct scaling behavior that persists across all device sizes. This is also evident in the total modal losses shown in Fig. 8(c). For the A-C modes, where lateral losses dominate, finite-CWT predicts higher losses than both kSWLE:CWT and kSWLE:GME at small radii, with the difference gradually diminishing at larger radii due to the steeper L-scaling. In contrast, the D-modes are primarily limited by vertical losses, and differences in lateral loss scaling become visible only at small device sizes, where lateral leakage becomes comparable to the large vertical losses of the D-modes.

To further investigate these differences, Fig. 9 shows the modal wavelength and loss values from both finite-CWT and kSWLE:CWT across a range of device radii. The wavelength in kSWLE was calculated by weighting the real part of $\omega(\mathbf{k})$ in analogy to Eq. (10). As expected, both methods converge toward the infinite-system values as L increases from 10 µm to 500 µm. However, the convergence trajectories differ. Finite-CWT exhibits systematically higher losses at small radii, reflecting differences in lateral loss modeling, deviations from the Gaussian mode assumption, and the increasing influence of mode mixing on the field composition. While both methods capture the same asymptotic behavior in larger devices, their treatment of lateral confinement leads to significant differences in the finite-size regime for small L.

5.4. Threshold gain predictions for finite devices

In this section, we extend the comparison between kSWLE (with CWT and GME input) and finite-CWT to predictions of the total modal loss for finite devices, which directly determines the required threshold gain. To achieve this, we examine how modal losses and lasing mode selection depend on device radius and fill factor, and how different treatments of finite-size effects influence these predictions.

Figure 10 illustrates how the predicted lasing mode changes with radius for several fill factors. Discrepancies occur over the whole length scale. In the small-radius regime, mode mixing and deviations from the Gaussian envelope assumed in kSWLE play a larger role. These effects are

Optics EXPRESS

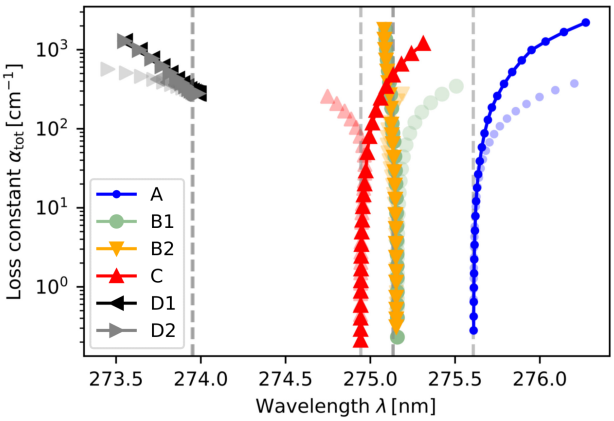

Fig. 9. Wavelength and loss rate, α_{tot} for each mode as obtained from finite-CWT (connected symbols) and kSWLE using CWT input (semi-transparent symbols), as the radius is varied from L =10 µm (highest loss) to L =500 µm (lowest loss).

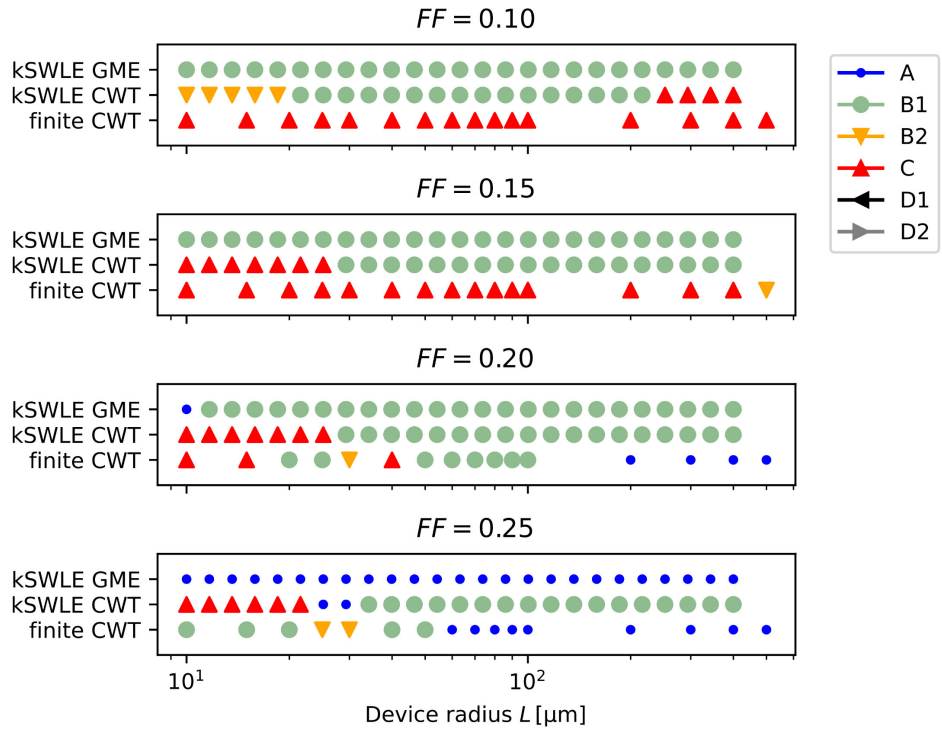

Fig. 10. Lowest-loss mode predicted by each method as a function of PCSEL radius L, for fill-factors FF = 10%, 15%, 20%, and 25%. Results are shown for kSWLE using GME input, kSWLE using CWT input, and full finite-CWT simulations.

implicitly modeled in finite-CWT, which solves for the full spatial field using a finite-difference approach on a hexagonal grid. For larger radii discrepancies arise from the different band structures of the infinite system, as predicted by the respective model.

Figure 11 compares total losses as a function of fill factor for a fixed radius of L = 100 µm. The C mode exhibits a monotonic increase in loss with increasing fill factor across all methods,

Optics EXPRESS

while the A mode shows a monotonic decrease. The B modes show a more complex behavior. In finite-CWT, B_1 and B_2 remain degenerate and exhibit a broad minimum in losses around $FF \approx 16\%$. In contrast, both kSWLE:CWT and kSWLE:GME predict a non-degenerate behavior: B_2 exhibits a similar broad minimum near $FF \approx 16\%$ to that seen in finite-CWT, while B_1 shows a steady increasing loss with increasing fill-factor.

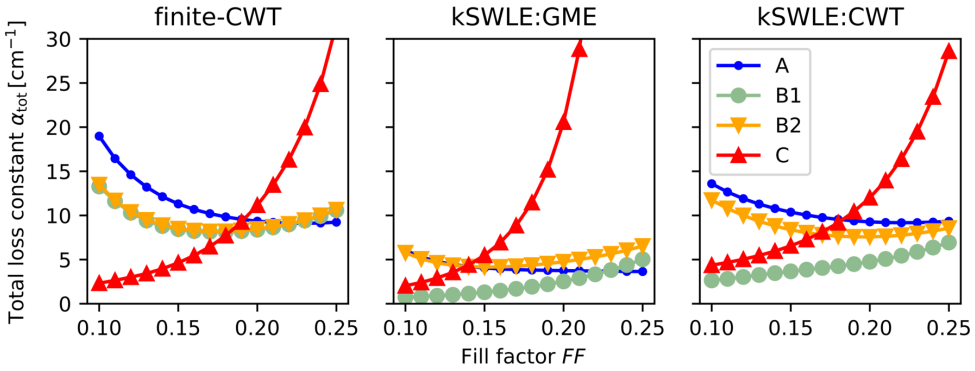

Fig. 11. Total modal loss, α_{tot}, as function of fill factor FF, at a fixed device radius of $L = 100$ µm, using different modelling approaches: (a) finite-CWT, (b) kSWLE with GME input, and (c) kSWLE with CWT input. Each panel shows how the predicted total loss varies with FF, and how the dominant low-loss mode may differ depending on the underlying bandstructure model and approximation method.

These differences arise from the directional dependence of dispersion and vertical loss away from the Γ-point, which influences the kSWLE estimates. Since kSWLE integrates over these properties, it is more sensitive to anisotropies in the bandstructure, especially in GME, which includes a more complete representation of higher-order effects. As a result, even within the same kSWLE framework, the choice of dispersion model (CWT or GME) significantly influences the predicted lasing behavior.

We note that while kSWLE provides a computationally efficient way to estimate losses based on infinite-structure data, its validity is limited to regimes where the finite mode can be clearly associated with a dominant band. As shown in Section S3 of the Supplementary, mode decomposition reveals that for small radii or specific fill factors, multiple bands may contribute significantly to a single mode. In such cases, the Gaussian spectral assumption breaks down, and neither kSWLE nor conventional finite-CWT can unambiguously separate vertical and lateral losses. These limitations highlight the need to validate loss estimates in regions where modal overlap is strong.

Overall, this comparison shows that kSWLE and finite-CWT offer complementary insights. The kSWLE model provides a transparent framework for estimating losses and exploring the impact of different bandstructure models. Finite-CWT, meanwhile, captures the full spatial complexity of the lasing mode and includes important finite-size effects such as mode-mixing and lateral field truncation. The observed differences between the two approaches do not imply that one is superior, but rather emphasize the importance of understanding the assumptions inherent in each model — especially when interpreting experimental results or designing PCSELs with small or intermediate aperture sizes.

6. Conclusions

We have presented a detailed comparison of methods for modeling finite-size effects in photonic-crystal surface-emitting lasers (PCSELs), focusing on how the choice of infinite-structure band model influences the estimation of vertical and lateral losses. Our work builds on the finite

Optics EXPRESS

coupled-wave theory (finite-CWT), which is the established simulation method for realistically sized PCSELs. However, its reliance on the simplified infinite-CWT model, which only includes a small subset of reciprocal lattice vectors, motivates the need for a more flexible framework.

To address this, we introduced the k-space weighted loss estimation (kSWLE) approach, which enables lateral and vertical loss contributions to be estimated from the bandstructure of any infinite model. We applied kSWLE using both CWT and GME bandstructures, and demonstrated that the predicted losses depend significantly on the choice of underlying model. This underlines the importance of accurate infinite-structure modeling, especially for strongly leaky modes or devices with small lateral size.

Comparison with full finite-CWT simulations shows that both finite-CWT and kSWLE agree well in many cases, despite the simplified assumptions of CWT. However, in parameter regimes where multiple bands contribute significantly to the lasing mode, the spectral distribution becomes ambiguous and mode classification breaks down. Mode decomposition analysis highlights this ambiguity, showing that in such cases, neither kSWLE nor finite-CWT can reliably isolate vertical and lateral losses.

Overall, kSWLE provides a computationally efficient alternative for estimating losses and exploring design trends. Its main strength lies in its flexibility: it can be used with any infinite-structure model and offers a straightforward way to connect bandstructure features to finite-size effects. While it does not replace finite-CWT, it serves as a valuable tool for parametric studies and model benchmarking.

Funding. Knut och Alice Wallenbergs Stiftelse (2020.0119).

Disclosures. The authors declare no conflicts of interest.

Data availability. The data that support the findings of this study are available from the corresponding author upon reasonable request.

Supplemental document. The supplementary information provides derivations of vertical and lateral losses in finite PCSELs using finite-CWT (S1), details of the Fourier-based mode decomposition method (S2), and a discussion of the limits of the kSWLE framework for small device sizes (S3). See Supplement 1 for supporting information.

References

1. S. Noda, M. Yoshida, T. Inoue, *et al.*, "Photonic-crystal surface-emitting lasers," Nat. Rev. Electr. Eng. **1**(12), 802–814 (2024).
2. S. Noda, T. Inoue, M. Yoshida, *et al.*, "High-power and high-beam-quality photonic-crystal surface-emitting lasers: a tutorial," Adv. Opt. Photonics **15**(4), 977–1032 (2023).
3. K. Emoto, T. Koizumi, M. Hirose, *et al.*, "Wide-bandgap GaN-based watt-class photonic-crystal lasers," Commun. Mater. **3**(1), 72 (2022).
4. S. Noda, K. Kitamura, T. Okino, *et al.*, "Photonic-crystal surface-emitting lasers: review and introduction of modulated-photonic crystals," IEEE J. Sel. Top. Quantum Electron. **23**(6), 1–7 (2017).
5. E. Torres, J. Ciers, N. Rebelo, *et al.*, "Ultraviolet-C vertical-cavity surface-emitting lasers with precise cavity length control," Laser Photonics Rev. **19**(13), 2402203 (2025).
6. M. Imada, A. Chutinan, S. Noda, *et al.*, "Multidirectionally distributed feedback photonic crystal lasers," Phys. Rev. B **65**(19), 195306 (2002).
7. Y. Liang, C. Peng, K. Sakai, *et al.*, "Three-dimensional coupled-wave analysis for square-lattice photonic crystal surface emitting lasers with transverse-electric polarization: finite-size effects," Opt. Express **20**(14), 15945–15961 (2012).
8. Y. Liang, C. Peng, K. Ishizaki, *et al.*, "Three-dimensional coupled-wave analysis for triangular-lattice photonic-crystal surface-emitting lasers with transverse-electric polarization," Opt. Express **21**(1), 565–580 (2013).
9. S. Zanotti, M. Minkov, D. Nigro, *et al.*, "Legume: A free implementation of the guided-mode expansion method for photonic crystal slabs," Comput. Phys. Commun. **304**, 109286 (2024).
10. L.-L. Lin, Z.-Y. Li, and K.-M. Ho, "Lattice symmetry applied in transfer-matrix methods for photonic crystals," J. Appl. Phys. **94**(2), 811–821 (2003).
11. B. Lang, P. D. Sewell, A. Vukovic, *et al.*, "Assessment and extension of rapid design tools for modeling photonic crystal surface-emitting lasers," J. Opt. Soc. Am. B **42**(5), 1123–1130 (2025).
12. K. S. Kunz and R. J. Luebbers, *The Finite Difference Time Domain Method for Electromagnetics* (CRC Press, Boca Raton, 2018).
13. H.-Y. Ryu, M. Notomi, and Y.-H. Lee, "Finite-difference time-domain investigation of band-edge resonant modes in finite-size two-dimensional photonic crystal slab," Phys. Rev. B **68**(4), 045209 (2003).

Optics EXPRESS

14. M. Yokoyama and S. Noda, "Finite-difference time-domain simulation of two-dimensional photonic crystal surface-emitting laser," Opt. Express **13**(8), 2869–2880 (2005).
15. Y. Liang, T. Okino, K. Kitamura, *et al.*, "Mode stability in photonic-crystal surface-emitting lasers with large κ 1DL," Appl. Phys. Lett. **104**(2), 021102 (2014).
16. J. Liu, D. Kim, Z. Bian, *et al.*, "Convergence criteria for probabilistic Markov chains modelling of photonic crystal surface emitting lasers," in *Novel In-Plane Semiconductor Lasers XXII*, vol. 12440 (SPIE, 2023), pp. 75–80.
17. J. Liu, Y. Gao, P. Ivanov, *et al.*, "Probabilistic Markov chain modeling of photonic crystal surface emitting lasers," Appl. Phys. Lett. **123**(26), 261107 (2023).
18. J. Liu, X. Zhao, Z. Bian, *et al.*, "Optimization of pumping geometry of photonic crystal surface emitting lasers," in *Physics and Simulation of Optoelectronic Devices XXXIII*, vol. 13360 (SPIE, 2025), pp. 14–18.
19. Z. Bian, X. Zhao, J. Liu, *et al.*, "Resonator embedded photonic crystal surface emitting lasers," npj Nanophotonics **1**(1), 13 (2024).
20. D. Apaydın, H. Andersson, L. Uhlig, *et al.*, "Deep-uv photonic crystal surface-emitting lasers," Laser & Photonics Reviews p. e00271 (2025).;
21. D. Apaydin, J. Ciers, H. Andersson, *et al.*, "Optically pumped UVC photonic crystal surface-emitting laser," in *International Workshop on Ultraviolet Materials and Devices*, (2023). We-B4.3.
22. U. T. Schwarz, D. Apaydin, L. Persson, *et al.*, "Critical discussion of loss mechanisms in UV-C PCSEL," in *Novel In-Plane Semiconductor Lasers XXIV*, vol. PC13385 (SPIE, 2025), p. PC1338502.
23. K. Sakai, J. Yue, and S. Noda, "Coupled-wave model for triangular-lattice photonic crystal with transverse electric polarization," Opt. Express **16**(9), 6033–6040 (2008).
24. G. Cardinali, S. Kölle, A. Schulz, *et al.*, "Gain characteristics of optically pumped UVC lasers with wide AlGaN single-quantum-well active regions," Phys. Status Solidi A **221**(21), 2400067 (2024).
25. M. J. Bergmann and H. C. Casey, "Optical-field calculations for lossy multiple-layer $Al_xGa_{1-x}N/In_xGa_{1-x}N$ laser diodes," J. Appl. Phys. **84**(3), 1196–1203 (1998).
26. B. Witzigmann, F. Römer, M. Martens, *et al.*, "Calculation of optical gain in AlGaN quantum wells for ultraviolet emission," AIP Adv. **10**(9), 095307 (2020).
27. C. Reich, M. Guttmann, M. Feneberg, *et al.*, "Strongly transverse-electric-polarized emission from deep ultraviolet AlGaN quantum well light emitting diodes," Appl. Phys. Lett. **107**(14), 142101 (2015).
28. W.-Y. He and C. T. Chan, "The emergence of dirac points in photonic crystals with mirror symmetry," Sci. Rep. **5**(1), 8186 (2015).